



## Shock-induced $\{11\bar{2}1\} \rightarrow \{11\bar{2}2\}$ double twinning in titanium

Ping Zhou<sup>a,1</sup>, Shun Xu<sup>b,1</sup>, Dawu Xiao<sup>c</sup>, Chunli Jiang<sup>a</sup>, Yin Hu<sup>a</sup>, Jian Wang<sup>b,\*</sup>

<sup>a</sup> Science and Technology on Surface Physics and Chemistry Laboratory, Jiangyou, 621908, China

<sup>b</sup> Department of Mechanical and Materials Engineering, University of Nebraska-Lincoln, Lincoln, NE, 68588, USA

<sup>c</sup> The Institute of Materials, China Academy of Engineering Physics (CAEP), Jiangyou, 621907, China



### ARTICLE INFO

#### Keywords:

Titanium  
High strain rate  
Double twinning  
Dislocations

### ABSTRACT

Six twinning modes have been reported in  $\alpha$ -titanium, including three extension twinning modes  $\{10\bar{1}2\}$ ,  $\{11\bar{2}1\}$  and  $\{11\bar{2}3\}$  and three compression twinning modes  $\{11\bar{2}2\}$ ,  $\{11\bar{2}4\}$  and  $\{10\bar{1}1\}$ .  $\{10\bar{1}2\}$  and  $\{11\bar{2}2\}$  twins are frequently observed without strong dependence on strain rate, while  $\{11\bar{2}1\}$  and  $\{11\bar{2}4\}$  twins are observed at high strain rate. These twinning modes and their interactions such as double twinning play significant roles in determining mechanical properties and texture evolution of  $\alpha$ -titanium. In this work, we study double twinning associated with  $\{11\bar{2}1\}$  primary twin. In order to activate  $\{11\bar{2}1\}$  twinning, a split Hopkinson pressure bar (SHPB) device was adopted to conduct high strain rate ( $\sim 2600 \text{ s}^{-1}$ ) compression of high purity titanium along the extrusion direction. We observed 453  $\{11\bar{2}1\} \rightarrow \{11\bar{2}2\}$  double twins but zero  $\{11\bar{2}1\} \rightarrow \{11\bar{2}4\}$  double twins in six grains. Crystallographic analysis enables the classification of  $\{11\bar{2}1\} \rightarrow \{11\bar{2}2\}$  double twins into Group I ( $29.5^\circ < \bar{1}100 >$ ), Group II ( $55^\circ < 5\bar{5}10\bar{3} >$ ), Group III ( $80.6^\circ < \bar{1}100 >$ ) and Group IV ( $86.8^\circ < \bar{5}15\bar{1}0\bar{3} >$ ) according to the misorientation angle and axis pair. Groups I and II dominate in the proportion of experimentally detected double twins while Groups III and IV take a small proportion. We account for these phenomena according to apparent Schmid factor, modified deformation gradient accommodation, and twin nucleation via dislocation dissociation. The results demonstrate that the preferred secondary twinning mode and corresponding variant would, to the greatest extent, relax plastic deformation associated with the primary twinning.

### 1. Introduction

Deformation twinning plays significant role in mechanical properties and texture evolution of hexagonal metals such as magnesium, zirconium and titanium that has hexagonal close packed structure (HCP) (Christian and Mahajan, 1995; Partridge, 1967). Twinning accommodates strains along the  $c$ -axis, cooperating with and competing against non-basal slips (Sandlöbes et al., 2013; Thornburg and Piehler, 1975; Xie et al., 2016; Yoo et al., 2002; Zecevic et al., 2018). In  $\alpha$ -titanium, six twinning modes have been reported, three extension twinning modes  $\{10\bar{1}2\} < \bar{1}011 >$ ,  $\{11\bar{2}1\} < \bar{1}\bar{1}26 >$  and  $\{11\bar{2}3\} < \bar{1}\bar{1}22 >$  (referred to as  $T_i^I$ ,  $T_i^{II}$  and  $T_i^{III}$ , respectively) and three compression twinning modes  $\{11\bar{2}2\} < 11\bar{2}3 >$ ,  $\{11\bar{2}4\} < 22\bar{4}3 >$  and  $\{10\bar{1}1\} < 10\bar{1}2 >$  (referred to as  $C_i^I$ ,  $C_i^{II}$  and  $C_i^{III}$  respectively) (M.H. Yoo, 1981; Partridge, 1967; Xu et al., 2012). The subscript ‘ $i$ ’ represents six variants associated with each twinning mode and follows the definition in Ref (Xu et al., 2017a). Compression twinning is activated under compression along the  $c$ -axis (Qin and Jonas, 2014; Qin et al., 2014) or tension perpendicular to the  $c$ -axis (Mullins and Patchett, 1981; Roth et al., 2014). Opposite loadings will favour extension twinning (Hong et al., 2010, 2011; Park et al., 2012; Xin et al., 2012; Zambaldi et al.,

\* Corresponding author.

E-mail address: [jianwang@unl.edu](mailto:jianwang@unl.edu) (J. Wang).

<sup>1</sup> Dr. P. Zhou and Dr. S. Xu contributed equally to this work.

2015). The effect of grain size (Ghaderi and Barnett, 2011), strain rate (Ghosh et al., 2016; Khan et al., 2004, 2012; Khan and Yu, 2012; Shahba and Ghosh, 2016) and temperature (Khan et al., 2007; Oberson and Ankem, 2009) on the plastic deformation is investigated in titanium and its alloys.  $\{10\bar{1}2\} < \bar{1}011 > (T_i^I)$  and  $\{11\bar{2}2\} < 11\bar{2}3 > (C_i^I)$  twins are frequently observed without strong dependence on strain rate (Bao et al., 2013; Bozzolo et al., 2010; Ghaderi and Barnett, 2011; Qin and Jonas, 2014; Stanford et al., 2008; Tirry et al., 2011).  $\{11\bar{2}1\} < \bar{1}126 > (T_i^{II})$  and  $\{11\bar{2}4\} < 22\bar{4}3 > (C_i^{II})$  twins are often observed at high strain rate (Jin et al., 2016; Lainé and Knowles, 2015; Vaidya and Mahajan, 1980; Wang et al., 2013, 2015; Xu et al., 2012, 2017a; Zhou et al., 2017). The other two twinning modes,  $\{11\bar{2}3\} < \bar{1}122 > (T_i^{III})$  and  $\{10\bar{1}1\} < 10\bar{1}2 > (C_i^{III})$ , are rarely observed. Overall, twinning in  $\alpha$ -titanium is more prevalent at high strain rate (Christian and Mahajan, 1995; Gurao et al., 2011; Nemat-Nasser et al., 1999; Wyatt et al., 2012), causing increased strain-hardening (Chichili et al., 1998; Salem et al., 2003, 2005).

Each twinning mode has six equivalent variants due to the symmetry of hexagonal close packed structure. Multiple twin variants associated with the same or different twinning modes can be activated contemporaneously or sequentially and interact with each other (El Kadiri et al., 2013; Xu et al., 2017b; Yu et al., 2014a, 2014b). A considerable amount of work has been devoted to understanding the mechanisms and mechanics of twin-twin interactions (Morrow et al., 2014a, 2014b; Sim et al., 2018; Wang et al., 2013a; Xu et al., 2017a; Yu et al., 2011, 2014a). Double twinning is a sequential twinning process which involves the activation of a secondary twin inside one primary twin. In hexagonal metals, double twins can be grouped into two types according to the combination of primary and secondary twinning modes. One type is similar double twin, i.e., both primary and secondary twins are either compression or extension twins. The other is dissimilar double twin, i.e., one is compression twin and the other is extension twin. Dissimilar double twinning happens under monotonic loading while similar double twinning usually takes place under multi-directional loadings. For example, similar double twins  $\{10\bar{1}2\} \rightarrow \{10\bar{1}2\}$  are intensively generated in rolled AZ31 Mg plate when it is subjected to cyclic loading or strain path changes (Hong et al., 2011; Shi et al., 2015; Xin et al., 2012; Xu et al., 2013).

In  $\alpha$ -titanium, three extension twins and three compression twins may result in 18 dissimilar double twins. To date, Electron Backscatter Diffraction (EBSD) analysis and transmission electron microscopes (TEM) have revealed five dissimilar double twins, three compression  $\rightarrow$  tension double twins  $\{11\bar{2}2\} \rightarrow \{10\bar{1}2\} (C_i^I \rightarrow T_j^I)$ ,  $\{11\bar{2}2\} \rightarrow \{11\bar{2}1\} (C_i^I \rightarrow T_j^{II})$  and  $\{11\bar{2}4\} \rightarrow \{10\bar{1}2\} (C_i^{II} \rightarrow T_j^I)$ , and two tension  $\rightarrow$  compression double twins  $\{10\bar{1}2\} \rightarrow \{11\bar{2}2\} (T_i^I \rightarrow C_j^I)$  and  $\{11\bar{2}1\} \rightarrow \{11\bar{2}4\} (T_i^{II} \rightarrow C_j^{II})$ . Among them,  $\{11\bar{2}2\} \rightarrow \{10\bar{1}2\} (C_i^I \rightarrow T_j^I)$  double twins are most frequently observed at conventional strain rate (Chun et al., 2005; Salem et al., 2003; Xu et al., 2016, 2017c). Associated with formation of double twins, twinned region is reoriented with respect to the parent grain and twin-twin boundaries form, subsequently affecting twinning, de-twinning, and slip processes (Berghezan et al., 1961; Proust et al., 2007) and resulting increased strain hardening (Yu et al., 2011, 2015). Barnett et al. (2008) examined the activity of basal slip in the  $\{10\bar{1}1\} \rightarrow \{10\bar{1}2\}$  double twins in Mg and demonstrated that the maximal Schmid factor (SF) for basal slip in the majority of double twins is twice higher than that in the parent grain. Juan et al. (2012) studied internal stresses by using a double inclusion model based on Eshelbian micromechanics and found that SF analyses are not sufficient to correctly predict double twinning modes (Juan et al., 2012, 2014). From the viewpoint of crystallography, six secondary twin variants have the same misorientation with the primary twin, but they exhibit different misorientations in the macroscopic frame. Thus, the texture evolution associated with double twinning shows strong dependence on the selection of secondary twin variant (Won et al., 2016; Xu et al., 2017c).

Since twinning is significantly sensitive to strain rate, twin density increases with applied strain rate (Hazeli et al., 2018). At high strain rate,  $\{11\bar{2}1\} (T_i^{II})$  twins are often observed especially in coarse-grained  $\alpha$ -titanium (Lainé and Knowles, 2015; Xu et al., 2017a; Zhou et al., 2017). Inside primary twins  $\{11\bar{2}1\} T_i^{II}$ , three tension-compression double twins might be activated, including  $\{11\bar{2}1\} \rightarrow \{11\bar{2}2\} (T_i^{II} \rightarrow C_j^I)$ ,  $\{11\bar{2}1\} \rightarrow \{11\bar{2}4\} (T_i^{II} \rightarrow C_j^{II})$  and  $\{11\bar{2}1\} \rightarrow \{10\bar{1}1\} (T_i^{II} \rightarrow C_j^{III})$ . In this work, we study double twinning associated with primary twins  $\{11\bar{2}1\} T_i^{II}$  in  $\alpha$ -titanium.

In order to active  $\{11\bar{2}1\}$  twinning, a split Hopkinson pressure bar (SHPB) device was adopted to conduct high strain rate ( $\sim 2600s^{-1}$ ) compression along the axial direction of cylindrical-shaped high purity (99.995 wt. %) titanium samples. We observed  $\{11\bar{2}1\} \rightarrow \{11\bar{2}2\} (T_i^{II} \rightarrow C_j^I)$  double twins but no  $\{11\bar{2}1\} \rightarrow \{11\bar{2}4\} (T_i^{II} \rightarrow C_j^{II})$  and  $\{11\bar{2}1\} \rightarrow \{10\bar{1}1\} (T_i^{II} \rightarrow C_j^{III})$  double twins in our experiments. 453  $\{11\bar{2}1\} \rightarrow \{11\bar{2}2\}$  double twins are classified into four groups according to the misorientation between parent grain and secondary twin variants, and each group exhibits different activities. We also discuss the prevalence of  $\{11\bar{2}1\} \rightarrow \{11\bar{2}2\} (T_i^{II} \rightarrow C_j^I)$  double twins than  $\{11\bar{2}1\} \rightarrow \{11\bar{2}4\} (T_i^{II} \rightarrow C_j^{II})$  double twins based on the resultant deformation.  $\{10\bar{1}1\} (C_j^{III})$  twins are not considered here due to the poor activity at temperatures below 300 °C. We further supplement the variant selection principles of double twin (Xu et al., 2018) by adding the dislocation dissociation mechanisms of the pyramidal  $< c + a >$  slip for predicting double twins at high strain rate. The results demonstrate that the preferred secondary twin mode and corresponding variant would, to the greatest extent, relax plastic deformation associated with the primary twinning.

## 2. Experimental methods

The cylindrical-shaped high purity (99.995 wt. %) titanium with both diameter and length 6.3 mm was annealed in a vacuum of  $10^{-4}$  Pa at 800 °C for 1 h, then furnace cooled. A split Hopkinson pressure bar (SHPB) device was adopted to conduct high strain rate ( $\sim 2600s^{-1}$ ) compression along the axial direction of samples. The maximum strain was controlled to a low level of 6.6%. The adiabatic temperature rise in the samples is about 7 °C. Therefore, the effect of temperature on deformation mechanisms is negligible. A strain-stopper ring mounted on the outer circumference of sample controls the strain. The strain-stopper ring is set to inner diameter 6.85 mm and length 5.88 mm to ensure that the radial deformation is free from the constraints and the axial deformation reaches the expected strain. The contact regions among sample, SHPB and strain-stopper ring were lubricated by Vaseline to reduce friction. During SHPB loading, specimen length  $L_s$  (6.3 mm) is much smaller than the length of compression pulse  $2l$  ( $l$  is the length of

projectile of 150 mm) to ensure that the compression pulse can be reflected back and forth multiple times inside the sample. Firstly, the specimen undergoes compressive deformation once the compression wave reaches one end of the specimen. Subsequently, the specimen subjects tensile deformation once the compression wave arrives another end of the specimen and reflected as tension wave. Therefore, the specimen experienced complex stress and strain processes during a few microseconds of impact duration. Such a complicated loading process makes the microstructure under high strain rate different from low strain rate (Austin and McDowell, 2011; Xiang et al., 2018). More importantly, deformation modes are closely related to the deformation history inside the material. Here, we focus on double twinning associated with  $\{11\bar{2}1\}$  primary twinning.

The deformed sample was polished and EBSD mapping was carried out on the central region of longitudinal cross section, which was processed by low-speed diamond saw cutting. The surface for EBSD test was ground by SiC paper from grit 800# to 4000#, then polished for 30 min using colloidal silica, and finally etched for 2–5 s by Kroll reagent (volume ratio of HF:HNO<sub>3</sub>:H<sub>2</sub>O equals to 2:6:97). EBSD characterizations were conducted at 20 kV with a step size of 0.3 μm in a Sirion 200 scanning electron microscopy equipped with an EDAX/TEAM data acquisition system. The original EBSD data were analysed with software TSL OIM Analysis 7 and revealed complicated microstructural characters regarding twins.

### 3. $\{11\bar{2}1\} \rightarrow \{11\bar{2}2\}$ double twins

#### 3.1. Crystallographic features

For the easy description of  $\{11\bar{2}1\} \rightarrow \{11\bar{2}2\}$  double twins,  $\{11\bar{2}1\}$  and  $\{11\bar{2}2\}$  twin variants are presented as  $T_i^{II}$  and  $C_j^I$  where subscript  $i = 1 \dots 6$  represents twin variant. The subscript value increases in the counter clockwise direction, following the definition in Ref (Xu et al., 2017a). 36 combinations of  $T_i^{II} \rightarrow C_j^I$  can be classified into 4 groups according to their misorientations between secondary twin  $C_j^I$  and parent grain by rotating the orientation of the parent grain around the respective normal direction of primary and secondary twinning planes by 180°. According to the minimum misorientation angle and corresponding axis (the angle/axis pairs) between the parent and the 12 equivalent matrices of the secondary twin (Xu et al., 2017a), four groups of  $\{11\bar{2}1\} \rightarrow \{11\bar{2}2\}$  double twins have the angle/axis pairs of  $29.5^\circ \langle \bar{1}100 \rangle$ ,  $55^\circ \langle 5\ 5\ \bar{1}0\ 3 \rangle$ ,  $80.6^\circ \langle \bar{1}\bar{1}00 \rangle$  and  $86.8^\circ \langle \bar{5}\ 15\ \bar{1}0\ 3 \rangle$ , respectively.

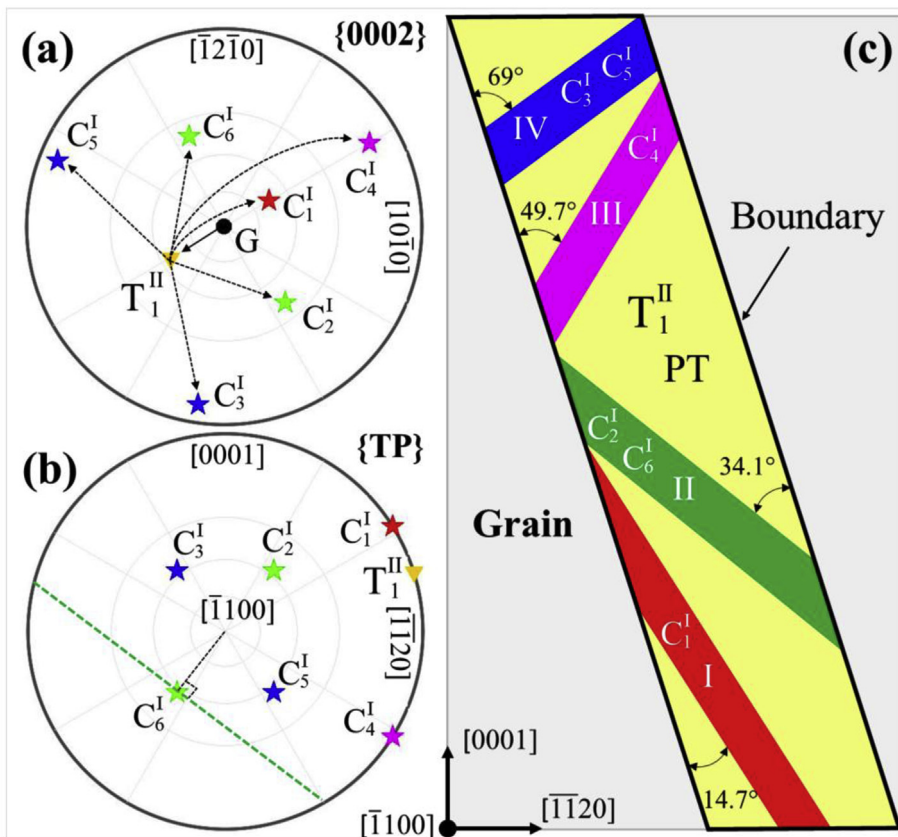
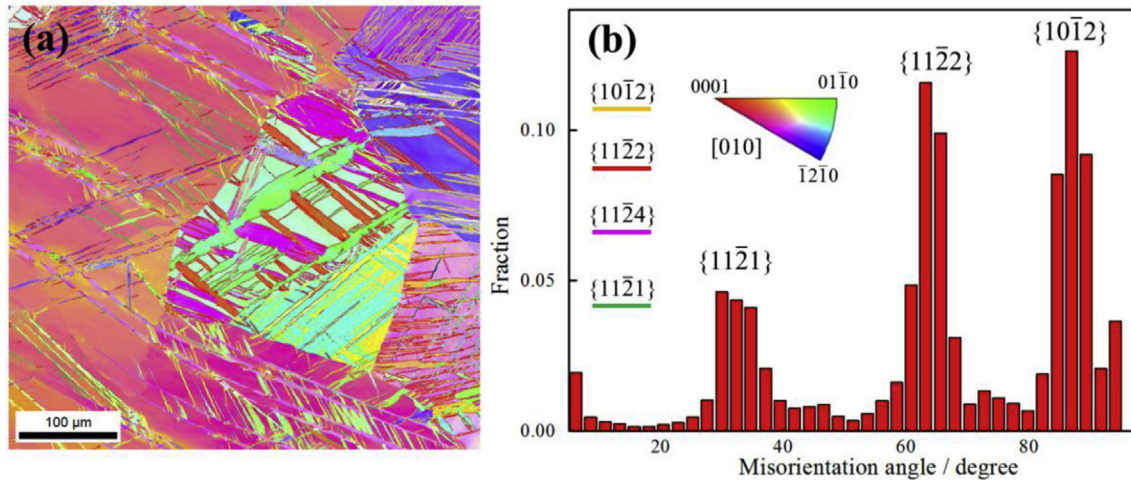


Fig. 1. (a)  $\{0002\}$  pole figure of a grain, a  $\{11\bar{2}1\}$  twin and six  $\{11\bar{2}2\}$  secondary twins in the coordinate of the grain: X ||  $[1010]$ , Y ||  $[\bar{1}210]$ , Z ||  $[0001]$ . The parent grain and the primary twin are presented by G and primary twin (PT), respectively. (b) Pole figure of the primary and secondary twinning planes in the coordinate in the primary twin: X ||  $[\bar{1}120]$ , Y ||  $[0001]$ , Z ||  $[\bar{1}100]$ . (c) An illustration map showing the traces of the primary and six secondary twinning planes in the coordinate set in (b).



**Fig. 2.** (a) A typical EBSD map of the sample deformed at high strain rate. Different colors are used to depict the twin boundaries: the green lines for  $\{11\bar{2}1\}$  twin boundaries, yellow for  $\{10\bar{1}2\}$ , red for  $\{11\bar{2}2\}$  and pink  $\{11\bar{2}4\}$ . (b) The grain-to-grain misorientation angle distribution corresponding to the map in (a). (For interpretation of the references to color in this figure legend, the reader is referred to the Web version of this article.)

In order to show the effect of secondary twin on the reorientation of basal poles,  $\{0002\}$  poles of the grain, the  $\{11\bar{2}1\}$  primary twin and six  $\{11\bar{2}2\}$  secondary twins are plotted into one pole figure (in Fig. 1a) that is established in the crystallographic frame of the grain with  $X \parallel [10\bar{1}0]$ ,  $Y \parallel [\bar{1}2\bar{1}0]$  and  $Z \parallel [0001]$ . The basal pole of the parent grain is represented by a black dot and located at the center of the pole figure. As a result of twinning, the basal pole of the  $\{11\bar{2}1\}$  primary twin (PT) is reoriented as marked by a yellow triangle. The basal poles of six variants of  $\{11\bar{2}2\}$  secondary twin inside the  $\{11\bar{2}1\}$  primary twin are shown by stars  $C_1^I$  in red (Group I),  $C_2^I$  and  $C_6^I$  in green (Group II),  $C_4^I$  in pink (Group III),  $C_3^I$  and  $C_5^I$  in blue (Group IV). For the convenience of distinguishing double twins in EBSD maps, we show the morphology of six secondary twins observed from the  $[\bar{1}100]$  zone axis. Fig. 1b depicts the projection of the normal of twinning planes into the coordinate in the primary twin where  $X \parallel [\bar{1}\bar{1}20]$ ,  $Y \parallel [0001]$ ,  $Z \parallel [\bar{1}100]$ . With this transformation, we can directly determine the trace of secondary twinning plane in the viewed direction. Take  $C_6^I$  for example, the green line represents the trace of  $C_6^I$  twinning plane in the observation plane. We then draw a  $C_6^I$  secondary twin in Fig. 1c. The green line in Fig. 1b is parallel to the trace of  $C_6^I$  twinning in Fig. 1c. Using this method, Fig. 1c schematically shows the geometrical relations between the primary and six secondary twinning traces on the observation direction. The angles between secondary twinning traces and the primary twinning plane are  $14.7^\circ$  for Group I,  $34.1^\circ$  for Group II,  $49.7^\circ$  for Group III and  $69^\circ$  for Group IV, respectively. Such geometrical features enable us to infer the group of double twins according to the twin morphology in EBSD maps.

### 3.2. EBSD observations

A typical EBSD map of the deformed sample in Fig. 2a shows plenty of twins. Corresponding to the crystallography of twins in titanium,  $\{11\bar{2}1\}$  tension twinning rotates the crystal by  $\sim 35^\circ$  around a  $\langle 1\bar{1}00 \rangle$  axis,  $\{11\bar{2}2\}$  compression twinning rotates the twinned domain by  $\sim 64^\circ$  around a  $\langle 1\bar{1}00 \rangle$  axis, and  $\{10\bar{1}2\}$  tension twinning results in a rotation of the crystal by  $\sim 87^\circ$  around a  $\langle 1\bar{2}10 \rangle$  axis. According to the misorientation axis and angle for each twin, specific colors are used to depict the twin boundaries as shown in Fig. 2a, i.e., green lines for  $\{11\bar{2}1\}$  twin boundaries, yellow lines for  $\{10\bar{1}2\}$  twin boundaries, and red lines for  $\{11\bar{2}2\}$  twin boundaries. The next-neighbor grain to grain misorientation corresponding to Fig. 2a is shown in Fig. 2b. The peaks at  $\sim 35^\circ$  and  $\sim 64^\circ$  are attributed to  $\{11\bar{2}1\}$  and  $\{11\bar{2}2\}$  twins, respectively.

Interestingly, many  $\{11\bar{2}1\} \rightarrow \{11\bar{2}2\}$  double twins are observed in our experiments. Fig. 3 presents an example of each group of double twins. In Fig. 3a, a typical orientation map indicating the predominant primary  $\{11\bar{2}1\}$  twins is taken in the grain with  $c$ -axis deviated  $46.6^\circ$  from the loading direction. One  $\{11\bar{2}1\}$  twin is labelled by a black arrow in Fig. 3a. Pole figure of the  $\{11\bar{2}1\}$  planes in Fig. 3f enables us to identify the primary twin to be  $T_6^{II}$  variant. Four square black boxes are used to indicate four groups of  $\{11\bar{2}1\} \rightarrow \{11\bar{2}2\}$  double twins, which are magnified in Fig. 3b–e. Corresponding pole figures of  $\{11\bar{2}2\}$  planes are plotted in Fig. 3b<sub>1</sub>–e<sub>1</sub>, which are used to determine the secondary twin variants by overlapping the  $\{11\bar{2}2\}$  poles of primary twin and the secondary twins. Taking Fig. 3b<sub>1</sub> for example, the  $(2\bar{1}\bar{1})$  plane has the smallest misalignment ( $1.12^\circ$ ) with the secondary twin. Therefore, the double twin in Fig. 3b can be described as  $T_6^{II} \rightarrow C_6^I$  double twin, which belongs to Group I. Similar analysis is applied to identify  $T_6^{II} \rightarrow C_1^I$  in Fig. 3c (Group II),  $T_6^{II} \rightarrow C_3^I$  in Fig. 3d (Group III) and  $T_6^{II} \rightarrow C_4^I$  in Fig. 3e (Group IV).

We identify 453  $T_6^{II} \rightarrow C_j^I$  double twins in six grains. In each grain, we characterized the number and variants of double twins and corresponding SFs of primary and secondary twins. The results are listed in Table 1. Four important phenomena are summarized as follows.

- a) **Variants relation:** Disregarding grains, Groups I and II dominate in the proportion of the totally detected 453 double twins, accounting for 60.5% and 33.8%, respectively. Group III and Group IV only take up 4.2% and 1.5%, respectively. In addition, the

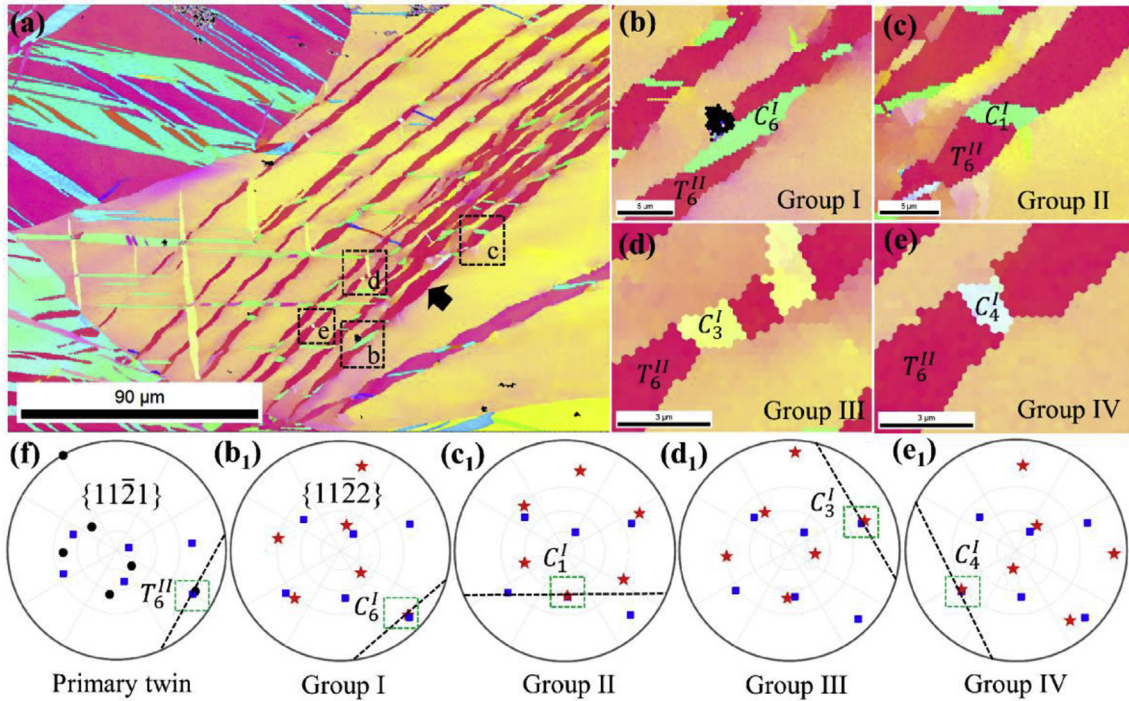


**Fig. 3.** (a) A typical EBSD map of the deformed sample. Four groups of  $T_6^{II} \rightarrow C_1^I$  double twins are magnified in (b): Group I, (c): Group II, (d): Group III and (e): Group IV. (f)  $\{11\bar{2}1\}$  pole figure of the parent grain and the primary twins as marked by a black arrows in (a). The corresponding  $\{11\bar{2}2\}$  pole figures of the four groups of double twins in (b<sub>1</sub>): Group I, (c<sub>1</sub>): Group II, (d<sub>1</sub>): Group III and (e<sub>1</sub>): Group IV. The black dots, blue squares and red stars represent the parent grains, primary twins and secondary twins. The traces of the twinning planes are depicted with dashed black lines in the pole figures. (For interpretation of the references to color in this figure legend, the reader is referred to the Web version of this article.)

**Table 1**

Statistical results of four groups of double twins in six parent grains named as A to F. The angle between the *c*-axis of the grain and the loading direction is indicated in blue, as well as the number of the observed double twins. PT1 and PT2 show the primary twin variant with the highest and second highest SF in each grain, respectively. SF of the double twin (DT) and the corresponding dislocation (Slip) that is needed for its nucleation by dislocation dissociation is also provided.

Parent grains	$\{11\bar{2}1\}$ Primary twins			Four groups of $\{11\bar{2}2\}$ double twins (453)									
	PT	No.	SF	I (274)		II (153)		III (19)		IV (7)			
				No.	SF	No.	SF	No.	SF	No.	SF		
				DT	Slip	DT	Slip						
A (40.4°)	PT1	4	0.39	8	0.49	0.20	7	0.49	0.48	0	0.34	0	0.42
	PT2	3	0.11	5	0.31	0.04	10	0.40	0.42	6	0.33	0	0.41
B (43.7°)	PT1	15	0.30	108	0.47	0.07	24	0.49	0.44	0	0.41	0	0.47
	PT2	2	0.18	3	0.34	0.38	2	0.42	0.44	8	0.36	0	0.43
C (46.6°)	PT1	11	0.41	22	0.49	0.24	16	0.49	0.49	0	0.48	3	0.43
	PT2	1	0.17	1	0.35	0.02	3	0.42	0.43	0	0.39	0	0.46
D (67.5°)	PT1	11	0.42	6	0.31	0.41	60	0.31	0.32	3	-0.01	2	0.30
	PT2	11	0.36	58	0.31	0.38	9	0.29	0.29	0	-0.14	0	0.28
E (68.9°)	PT1	5	0.44	0	0.35	0.40	2	0.35	0.36	0	-0.16	0	0.07
	PT2	5	0.36	6	0.34	0.34	2	0.32	0.31	0	0.02	0	0.31
F (70.5°)	PT1	5	0.43	2	0.33	0.42	16	0.34	0.35	2	0.08	2	0.34
	PT2	14	0.35	55	0.31	0.32	2	0.28	0.27	0	0.05	0	0.30

activity of four groups of double twins varies with grains as revealed in Table 1. When  $\{11\bar{2}1\}$  primary twins belong to one variant in the parent grain, Group I double twins are always preferred, especially in Grain B. When  $\{11\bar{2}1\}$  primary twins belong to two different variants (referred to as PT1 and PT2) in the parent grain, the activity of Group II double twins increases such as in Grain D and Grain F. For example, the EBSD map associated with grain D is shown in Fig. 4a and two regions are magnified in Fig. 4b and c. We identify secondary twin variants according to pole figures (Fig. 4d and e) of  $\{11\bar{2}1\}$  planes and  $\{11\bar{2}2\}$  planes associated with Fig. 4b. The dashed lines represent the trace of the twinning plane of the detected twins. The  $\{11\bar{2}1\} \rightarrow \{11\bar{2}2\}$  double twin in

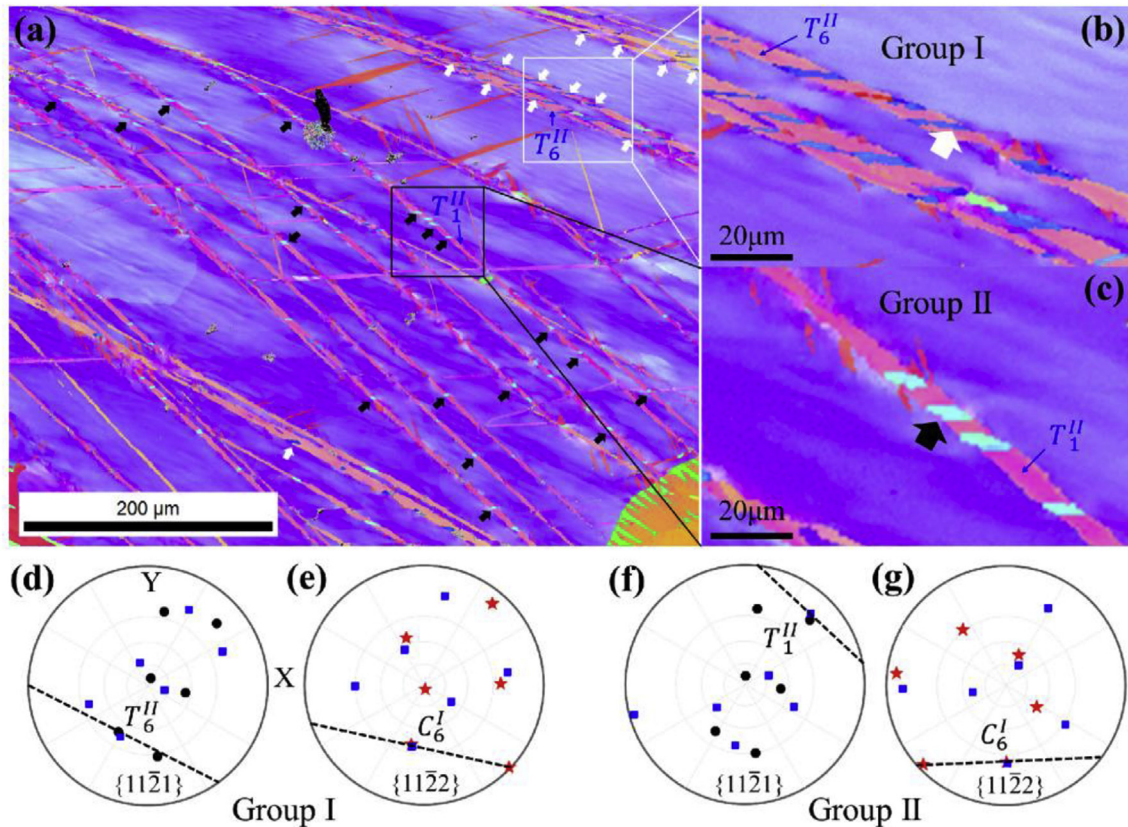


**Fig. 4.** (a) An EBSD map of the deformed sample showing (b) Group I and (c) Group II double twins. Pole figures of  $\{11\bar{2}1\}$  and  $\{11\bar{2}2\}$  twinning planes associated with Group I are presented in (d) and (e), respectively, and those associated with Group II are presented in (f) and (g), respectively. Black dots, blue squares and red stars represent the parent grain,  $\{11\bar{2}1\}$  primary twin and  $\{11\bar{2}2\}$  double twins, respectively. (For interpretation of the references to color in this figure legend, the reader is referred to the Web version of this article.)

- Fig. 4b is determined to be  $T_6^{\text{II}} \rightarrow C_6^{\text{I}}$ , which belongs to Group I. Some of these double twins are marked by white arrows in Fig. 4a. Similar analysis was done for double twins in Fig. 4c. Pole figures in Fig. 4f and g reveal that  $\{11\bar{2}1\} \rightarrow \{11\bar{2}2\}$  double twin in Fig. 4c can be described as  $T_1^{\text{II}} \rightarrow C_6^{\text{I}}$ , belonging to Group II. The EBSD analysis clearly reveals that Group I double twins (white arrows) are associated with  $T_6^{\text{II}}$  primary twin and Group II double twins (black arrows) are produced in  $T_1^{\text{II}}$  primary twin.
- b) **Stress influence on variant selection:** In all detected grains, two  $\{11\bar{2}1\}$  primary twins are activated with the highest and second highest SFs and are represented by PT1 and PT2 in Table 1, respectively. Therefore, the generation of  $\{11\bar{2}1\}$  primary twins obeys the SF law. It is noticed that more double twins are activated in PT1 twin that has higher SF. For example in Grain B, 132 double twins inside PT1 with a SF of 0.30 while only 13 double twins in PT2 with a SF of 0.18.
- c) **Orientation effect on variant selection:** Akhtar et al. (Akhtar, 1975) reported that  $\{11\bar{2}1\}$  twins tend to happen in single crystal titanium when the  $c$ -axis deviates from the tensile direction between  $47^\circ$  and  $60^\circ$ . The SF varies in a range between 0.37 and 0.49. The results indicate SF criterion works well for the variant selection of the  $\{11\bar{2}1\}$  twins in single crystal. In our polycrystalline Ti, the angles between the  $c$ -axis of each grain and the loading direction are not belonging to the angle range reported by Akhtar et al. (Akhtar, 1975). The SFs of the primary  $\{11\bar{2}1\}$  twins are between 0.11 and 0.44. More twins with comparatively lower SF are observed. We also noted that Group III double twins in grains D, E and F have quite lower SFs even negative SFs. These results must be accounted for by the heterogeneity of stresses inside grains in polycrystalline aggregate (Yang et al., 2011), because the local stress must favour the primary twins.
- d)  $\{11\bar{2}1\} \rightarrow \{11\bar{2}4\}$  double twins were not found in our EBSD data.

In summary, EBSD analysis reveals three interesting phenomena: 1)  $\{11\bar{2}1\} \rightarrow \{11\bar{2}2\}$  double twins are profuse when primary twin is  $\{11\bar{2}1\}$ , 2) Group I and Group II double twins prevail over others, and 3) Group II double twin becomes more popular when two different variants of  $\{11\bar{2}1\}$  primary twins are activated in one grain. In what follows, we address these observations according to apparent-SF, deformation gradient accommodation, and nucleation of secondary twins via dislocation dissociation.

#### 4. Discussion

Corresponding to a well-defined crystallography of double twins, three distinct principles have been proposed to predict variant

selection. Resolved shear stress associated with various twin variants can be estimated under the assumption of a positive resolved shear stress on primary twinning, and are used to predict variant selection (referred to as apparent SF or a-SF). However, SF analyses are not sufficient to correctly predict double twinning modes (Juan et al., 2012; Shi et al., 2015; Xu et al., 2018), as examined by using a double inclusion model for  $\{10\bar{1}1\} \rightarrow \{10\bar{1}2\}$  (Juan et al., 2012, 2014) and  $\{10\bar{1}2\} \rightarrow \{10\bar{1}2\}$  double twinning (Shi et al., 2015) in Mg. The displacement gradient based criteria have been developed to predict variant selection because displacement gradients associated with various twinning modes and variants can be calculated at the given crystallographic relation. Jonas et al. (Jonas et al., 2011; Mu et al., 2012; Qin and Jonas, 2014) proposed a displacement gradient accommodation (referred to as DGA) criterion to predict a primary twin variant. They transformed the displacement gradient tensor created by a primary twin into the crystal reference frame of the neighboring grain and then evaluated the accommodation through slips in the vicinity of the twin domain, demonstrating that the variant will be selected if basal slip is the best accommodative system. Xu et al. (2018) modified the DGA (referred to as m-DGA) for the variant prediction of secondary twinning inside a primary twin with a focus on minimizing the resultant plastic deformation in the matrix associated with double twinning. In other words, a selected secondary twin variant should, to the greatest extent, diminish the shear deformation resulting from the primary twin. With the focus on nucleation of secondary twin, the boundary of a primary twin acts as barriers for dislocation motion and facilitates dislocation dissociation at the boundary into twinning dislocations of secondary twins (referred to as NDD) (Beyerlein et al., 2012). Xu et al. (2018) recently made a systematic comparison of these criteria for variant selection in four types of double twins in titanium. They concluded that the a-SFs associated with secondary twins are always positive once the primary twin is activated, thus predicting no obvious preference for the selection of secondary twin variants; The m-DGA and NDD correctly predict the selection of secondary twin variants, implying that the preferred secondary twin variant would, to the greatest extent, relax plastic deformation associated with the primary twinning and the nucleation of the secondary twin variant is facilitated by the accumulation of available gliding dislocations at the primary twin boundary. It is worth noting that they only consider  $\langle a \rangle$  dislocations because it is easily activated in hexagonal metals at room temperature. Here we examine these principles for  $\{11\bar{2}1\} \rightarrow \{11\bar{2}2\}$  double twins and discuss the low activity of  $\{11\bar{2}1\} \rightarrow \{11\bar{2}4\}$  double twins.

#### 4.1. SF effect on selection of secondary twin variant

Apparent SF (a-SF) analysis is adopted to define stress states that favour the activation of primary and secondary twins. An inverse pole figure with X ||  $[10\bar{1}0]$ , Y ||  $[\bar{1}2\bar{1}0]$  and Z ||  $[0001]$  is set firstly. Primary twin  $T_1^{II}$  is chosen to conduct the a-SF analysis. All loadings that induce  $T_1^{II}$  twin with a SF larger than 0.3 are plotted into the inverse pole figure (Fig. 5a) under the assumption of uniaxial compression condition.

SFs of the six potential  $\{11\bar{2}2\}$  secondary twin variants  $C_j^I$  ( $j = 1 \dots 6$ ) inside  $T_1^{II}$  are calculated within the loading domain of primary twin  $T_1^{II}$ , as shown in Fig. 5b–g, where the red indicates positive SFs and the blue denotes negative SFs. The results show that twin variants  $C_1^I$  (Group I),  $C_2^I$  and  $C_6^I$  (Group II) always hold positive SFs, while variants  $C_4^I$  (Group III),  $C_3^I$  and  $C_5^I$  (Group IV) hold relatively lower or negative SFs under some loading directions, especially for Group III (blue color). It is also clearly shown in Fig. 5e that the SFs of Group III become smaller and even negative as the angle between the c-axis of the grain and the loading direction increases from  $60^\circ$  to  $90^\circ$ . In a brief summary, a-SF analysis is able to explain the high proportion of Group I and Group II and the low frequency of Group III and Group IV, but cannot distinguish the preference between Group I and Group II. Similar analysis for  $\{11\bar{2}4\}$  secondary twins inside primary  $\{11\bar{2}1\}$  twins shows that  $\{11\bar{2}4\}$  secondary twins are favorable according to their SFs (Xu et al., 2018).

#### 4.2. Deformation associated with $\{11\bar{2}2\}$ and $\{11\bar{2}4\}$ secondary twinning

The modified DGA criterion (m-DGA) based on minimizing the resultant plastic deformation associated with the double twinning was found more effective to predict the variant selection of secondary twins (Xu et al., 2018). In this method, the displacement gradient associated with six secondary twin variants is transformed into the twinning reference frame of the primary twin, which is set up as: 1-direction || shear direction of the primary twin, 3-direction || twinning plane normal, and 2-direction is the cross product of 3-direction and 1-direction. Therefore,  $e_{13}$  component of the rotated tensor indicates the displacement gradient that happens along the shear direction on the twinning plane of the primary twin. A larger magnitude of the  $e_{13}$  component (light blue) will more effectively diminish the resultant strain of the primary twin. In  $\{11\bar{2}1\}$  primary twins, both  $\{11\bar{2}2\}$  and  $\{11\bar{2}4\}$  are potential double twinning systems. Table 2 summarizes the displacement gradient tensors of six  $\{11\bar{2}4\}$  and six  $\{11\bar{2}2\}$  secondary twins that are transformed into the twinning reference frame of the  $(11\bar{2}1)[\bar{1}126]$  primary twin. It can be seen that the comparatively effective value is  $-0.2058$  for  $T_1^{II} \rightarrow C_1^I$  and  $-0.11$  for  $T_1^{II} \rightarrow C_{i+1}^I$  and  $C_{i+5}^I$ , while  $-0.1509$  for  $T_1^{II} \rightarrow C_i^{II}$  and  $-0.0831$  for  $T_1^{II} \rightarrow C_{i+1}^{II}$  and  $C_{i+5}^{II}$ . Therefore,  $\{11\bar{2}2\}$  secondary twinning is more beneficial to diminish the strain associated with  $\{11\bar{2}1\}$  primary twin, compared to  $\{11\bar{2}4\}$  secondary twins. This could be one reason why  $\{11\bar{2}1\} \rightarrow \{11\bar{2}2\}$  double twinning prevails over  $\{11\bar{2}1\} \rightarrow \{11\bar{2}4\}$  double twinning.

In addition, m-DGA analysis for six  $\{11\bar{2}2\}$  twin variants reveals that Group I ( $T_1^{II} \rightarrow C_1^I$ ) and Group II ( $T_1^{II} \rightarrow C_{i+1}^I$ ,  $T_1^{II} \rightarrow C_{i+5}^I$ ) are more effective in diminishing the resultant strain than other two groups. Especially, Group I ( $T_1^{II} \rightarrow C_1^I$ ) is relatively preferred than Group II ( $T_1^{II} \rightarrow C_{i+1}^I$ ,  $T_1^{II} \rightarrow C_{i+5}^I$ ) because of the largest  $e_{13}$  value. EBSD results confirm that Group I double twins prevail over others when a grain only contains  $\{11\bar{2}1\}$  primary twins. However, Group II obviously shows an increased activity in grains that have two different primary twin variants. In this case, Group I double twins are favorable in one primary twin and Group II are popular in the other primary twin. This could be due to spatially heterogeneous stresses in the grain.

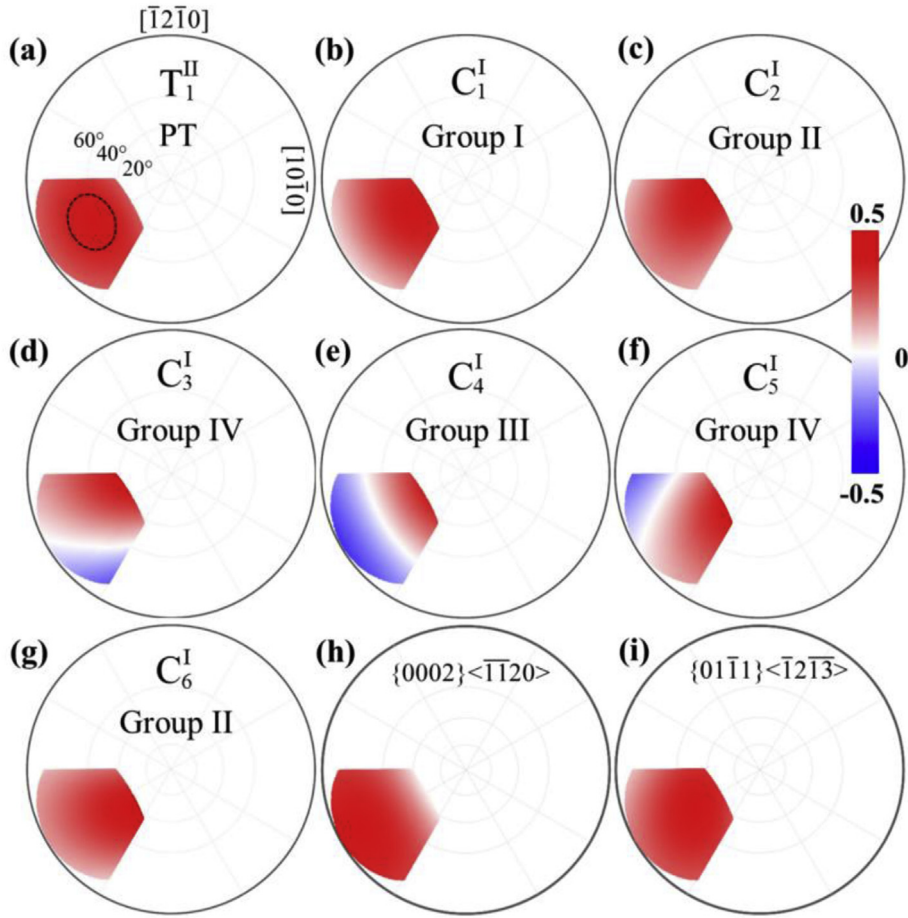
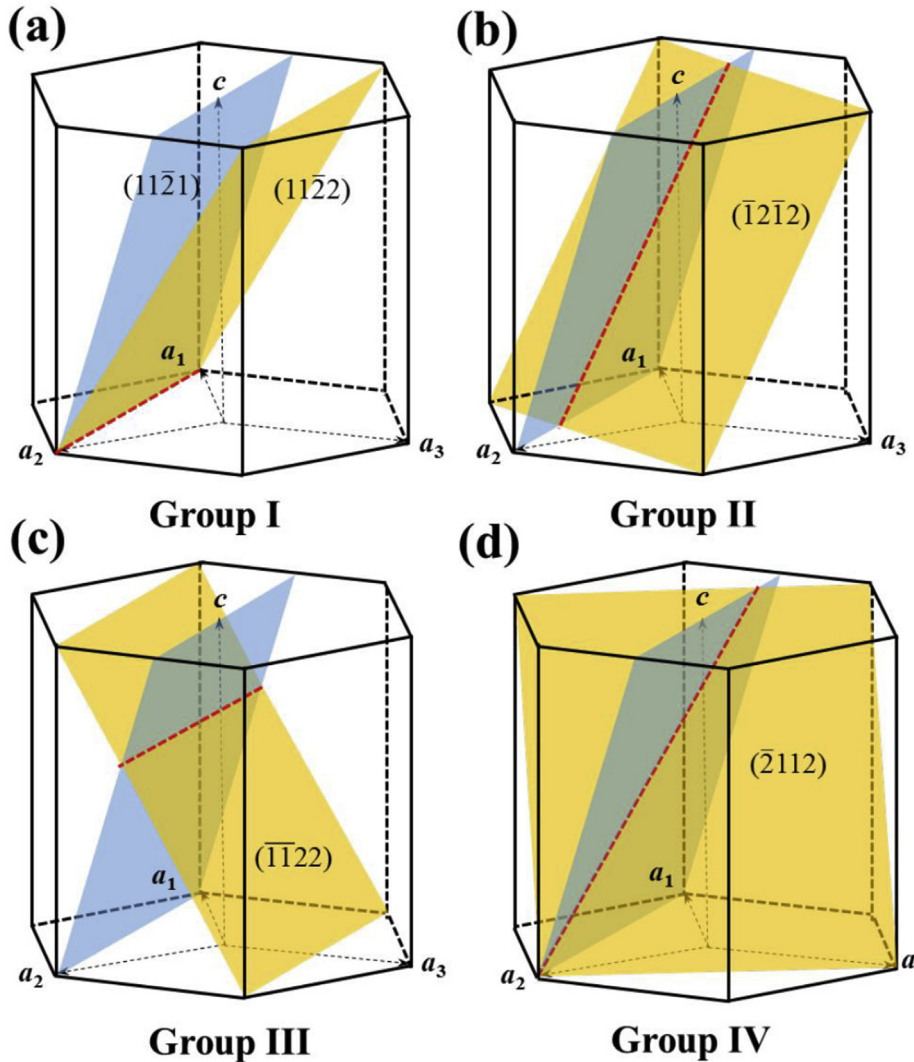


Fig. 5. a-SF analysis of primary twin  $T_1^{II}$  and secondary twin  $C_1^I$ . (a) LDs domain with SFs larger than 0.3 for primary twin  $T_1^{II}$ . (b)–(i) SF distributions for six secondary  $C_1^I$ ,  $\{0002\} \langle 1120 \rangle$  and  $\{0111\} \langle 1213 \rangle$  slip in LD domains determined by primary twins  $T_1^{II}$ .

Table 2

Rotation of the displacement gradient tensors associated with six potential  $\{11\bar{2}2\}$  and six  $\{11\bar{2}4\}$  secondary twins into the twinning reference frame of the  $(11\bar{2}1)[\bar{1}126]$  primary twin.

$\{11\bar{2}1\} \rightarrow \{11\bar{2}2\}$	m-DGA	$\{11\bar{2}1\} \rightarrow \{11\bar{2}4\}$	m-DGA
$(11\bar{2}2)[11\bar{2}3]$ $T_i^{II} \rightarrow C_i^I$	$\begin{bmatrix} -0.0541 & 0 & -0.2058 \\ 0 & 0 & 0 \\ 0.0142 & 0 & 0.0541 \end{bmatrix}$	$(11\bar{2}4)[22\bar{4}3]$ $T_i^{II} \rightarrow C_i^{II}$	$\begin{bmatrix} -0.1021 & 0 & -0.1509 \\ 0 & 0 & 0 \\ 0.0691 & 0 & 0.1021 \end{bmatrix}$
$(\bar{1}\bar{2}\bar{1}2)[\bar{1}\bar{2}\bar{1}3]$ $T_i^{II} \rightarrow C_{i+1}^I$	$\begin{bmatrix} -0.0744 & 0.143 & -0.11 \\ -0.0387 & 0.0744 & -0.0572 \\ 0 & 0 & 0 \end{bmatrix}$	$(\bar{1}\bar{2}\bar{1}4)[\bar{2}\bar{4}\bar{2}3]$ $T_i^{II} \rightarrow C_{i+1}^{II}$	$\begin{bmatrix} -0.1022 & 0.0842 & -0.0831 \\ -0.0976 & 0.0803 & -0.0794 \\ 0.0269 & -0.0221 & 0.0219 \end{bmatrix}$
$(\bar{2}112)[\bar{2}11\bar{3}]$ $T_i^{II} \rightarrow C_{i+2}^I$	$\begin{bmatrix} -0.1016 & 0.1172 & 0.0389 \\ -0.0645 & 0.0744 & 0.0247 \\ -0.0711 & 0.082 & 0.0272 \end{bmatrix}$	$(\bar{2}114)[\bar{4}2\bar{2}3]$ $T_i^{II} \rightarrow C_{i+2}^{II}$	$\begin{bmatrix} -0.0879 & 0.0563 & 0.0064 \\ -0.1254 & 0.0803 & 0.0091 \\ -0.1036 & -0.0664 & 0.0075 \end{bmatrix}$
$(\bar{1}\bar{1}22)[\bar{1}\bar{1}2\bar{3}]$ $T_i^{II} \rightarrow C_{i+3}^I$	$\begin{bmatrix} -0.1085 & 0 & 0.0921 \\ 0 & 0 & 0 \\ -0.1279 & 0 & 0.1085 \end{bmatrix}$	$(\bar{1}\bar{1}24)[\bar{2}\bar{2}4\bar{3}]$ $T_i^{II} \rightarrow C_{i+3}^{II}$	$\begin{bmatrix} -0.0735 & 0 & 0.0281 \\ 0 & 0 & 0 \\ -0.1919 & 0 & 0.0735 \end{bmatrix}$
$(1\bar{1}\bar{2}12)[1\bar{1}\bar{2}1\bar{3}]$ $T_i^{II} \rightarrow C_{i+4}^I$	$\begin{bmatrix} -0.1016 & -0.1172 & 0.0389 \\ 0.0645 & 0.0744 & -0.0247 \\ -0.0711 & -0.082 & 0.0272 \end{bmatrix}$	$(1\bar{1}\bar{2}14)[2\bar{4}2\bar{3}]$ $T_i^{II} \rightarrow C_{i+4}^{II}$	$\begin{bmatrix} -0.0879 & -0.0563 & 0.0064 \\ 0.1254 & 0.0803 & -0.0091 \\ -0.1036 & -0.0664 & 0.0075 \end{bmatrix}$
$(2\bar{1}\bar{1}2)[2\bar{1}\bar{1}3]$ $T_i^{II} \rightarrow C_{i+5}^I$	$\begin{bmatrix} -0.0744 & -0.143 & -0.11 \\ 0.0387 & 0.0744 & 0.0572 \\ 0 & 0 & 0 \end{bmatrix}$	$(2\bar{1}\bar{1}4)[4\bar{2}\bar{2}3]$ $T_i^{II} \rightarrow C_{i+5}^{II}$	$\begin{bmatrix} -0.1022 & -0.0842 & -0.0831 \\ 0.0976 & 0.0803 & 0.0794 \\ 0.0269 & 0.0221 & 0.0219 \end{bmatrix}$



**Fig. 6.** Crystallography of four groups of  $\{11\bar{2}1\} \rightarrow \{11\bar{2}2\}$  double twins. Blue plane represents the primary  $\{11\bar{2}1\}$  twinning plane, orange plane represents the secondary  $\{11\bar{2}2\}$  twin plane, red dashed line denotes the intersection line between the primary twinning plane and four groups of secondary twinning planes. (For interpretation of the references to color in this figure legend, the reader is referred to the Web version of this article.)

### 4.3. Nucleation of secondary twins

Once a twin forms, the twin boundary is the barrier to dislocations, resulting in the accumulation and reaction of dislocations at the twin boundary (Ardeljan et al., 2017; Fan et al., 2015; Gong et al., 2018; Wang and Agnew, 2016; Wang et al., 2013b). Recently, Beyerlein et al. (2012) and Xu et al. (2018) proposed that formation of double twins could be evoked by gliding dislocation interaction with primary twin boundary. Recently, Xu et al. analysed the nucleation of  $\{11\bar{2}4\}$  secondary twins inside primary  $\{11\bar{2}1\}$  twins (Xu et al., 2018), indicating that the reaction of basal  $\langle a \rangle$  at primary twin boundary can also mediate the nucleation of  $\{11\bar{2}4\}$  double twins. Here we analyze the nucleation of  $\{11\bar{2}2\}$  secondary twins inside primary  $\{11\bar{2}1\}$  twins. Fig. 6 shows the geometric relation between primary twinning plane  $\{11\bar{2}1\}$  (blue) and secondary twinning planes  $\{11\bar{2}2\}$  (orange). Red dash lines indicate the intersection lines between secondary twin planes and the primary twin plane. The intersection line associated with Group I and Group III double twins aligns with  $[\bar{1}100]$  which lies on the basal plane (Fig. 6a and c). For Group II, the intersection line is parallel to the twinning direction of the secondary twinning variants, i.e.  $[\bar{1}2\bar{1}3]$  for  $C_2^I$  and  $[2\bar{1}13]$  for  $C_6^I$ , which lie on  $\{10\bar{1}1\}$  pyramidal plane. For Group IV, the intersection line is along  $\langle 2\bar{3}13 \rangle$ , which does not lie on any usual slip planes (Fig. 6d).

Assuming twin nucleation via dislocation dissociation at primary twin boundary, the nucleation of Group I and III double twins can be facilitated by the dissociation of basal  $\langle a \rangle$  dislocation (Beyerlein et al., 2012; Mendelson, 1969, 1970). An  $\langle a \rangle$  dislocation with Burgers vector  $b_i$  can be dissociated into  $x$  secondary twinning dislocations  $xb_i^m$  and a residual dislocation  $b_r^m$ , where the subscript  $m$  represents secondary twin variant  $C_m^I$ . This process can be described as  $b_i \Rightarrow xb_i^m + b_r^m$ .  $b_i = a_i$  with a magnitude of

**Table 3**

Nucleation of the secondary twin variants  $\{11\bar{2}2\}$  inside the primary twin  $(11\bar{2}1)[11\bar{2}6]$ .

Secondary twin	$b_i$	$b_i$	$b_i^m$	$ b_i ^2$	$x$	$ xb_i ^2$	$ b_i^m ^2$
$C_1^I$	$\lambda[11\bar{2}3]$	$b_1$	$[0.72 \ 0.28 \ 0.44 \ 0.15]$	8.7	1	0.67	10.66
		$b_2$	$[0.28 \ 0.72 \ 0.44 \ 0.15]$	8.7	1	0.67	10.66
		$b_3$	$[0.28 \ 0.28 \ 0.56 \ 0.15]$	8.7	1	0.67	6.80
$C_2^I$	$\lambda[\bar{1}2\bar{1}3]$	$c + b_2$	$[0.04 \ 0.08 \ 0.04 \ 0.11]$	30.63	6	24.12	0.4
$C_4^I$	$\lambda[\bar{1}\bar{1}2\bar{3}]$	$b_1$	$[0.72 \ 0.28 \ 0.44 \ 0.15]$	8.7	1	0.67	10.66
		$b_2$	$[0.28 \ 0.72 \ 0.44 \ 0.15]$	8.7	1	0.67	10.66
		$b_3$	$[0.38 \ 0.38 \ 0.76 \ 0.15]$	8.7	1	0.67	11.94
$C_6^I$	$\lambda[2\bar{1}\bar{1}3]$	$c + b_1$	$[0.08 \ 0.04 \ 0.04 \ 0.11]$	30.63	6	24.12	0.4

0.295 nm for  $\alpha$ -Ti. The three vectors  $\mathbf{a}_1$ ,  $\mathbf{a}_2$ , and  $\mathbf{a}_3$  are equal to  $\frac{1}{3}[2\bar{1}10]$ ,  $\frac{1}{3}[\bar{1}210]$  and  $\frac{1}{3}[\bar{1}\bar{1}20]$ , respectively. The Burgers vector of  $\{11\bar{2}2\}$  TD  $\mathbf{b}_i^m = \lambda < 11\bar{2}3 >$ ,  $\lambda = \frac{k^2-2}{k^2+1} = 0.1477$  for Ti ( $a = 0.295$  nm and  $c = 0.4683$  nm,  $k = c/a$ ). The results associated with the dislocation dissociation are listed in Table 3. The number  $x$  is the maximum allowable number of twinning dislocations according to Frank's law. For  $C_1^I$  and  $C_4^I$  secondary twins, three  $< \mathbf{a} >$  dislocations on basal plane can act as sources for the dissociation. SF of the corresponding  $\mathbf{b}_i$  dislocation is listed in Table 1. It is noted that only the dissociation of  $\mathbf{b}_3$  dislocation is energetically favorable for producing twinning dislocation of secondary twin variant  $C_1^I$ , indicating that the formation of Group I double twins is favored while Group III is unlikely. This is consistent with experimental observations.

For Group II, the intersection line lies on  $\{10\bar{1}1\}$  pyramidal plane. One can speculate that twinning dislocations can be produced through the dissociation of pyramidal  $< \mathbf{c} + \mathbf{a} >$  dislocation, i.e.,  $b_{< \mathbf{c} + \mathbf{a} >} \Rightarrow xb_i^m + b_i^m$ . A  $b_{< \mathbf{c} + \mathbf{a} >} = \frac{1}{3}[\bar{1}2\bar{1}3]$  dislocation on the pyramidal plane can produce six twinning dislocations ( $x = 6$ ) according to Frank's law ( $|b_{< \mathbf{c} + \mathbf{a} >}|^2 > |b_i^m|^2 + |xb_i^{(12\bar{1}2)}|^2$ ). The SF of  $\{01\bar{1}1\} < \bar{1}2\bar{1}3 >$  slip within  $\{11\bar{2}1\}$  primary twin is presented in Fig. 5i. It indicates that the stress state favoring  $T_1^{II}$  primary twin also facilitates nucleation and glide of  $\{01\bar{1}1\} < \bar{1}2\bar{1}3 >$  slip.

In the detected primary twins, the SF of  $\{01\bar{1}1\} < \bar{1}2\bar{1}3 >$  slip associated with the nucleation of Group II double twins is always great, favoring the glide of  $01\bar{1}1 < \bar{1}2\bar{1}3 >$  dislocations. Vaidya and Mahajan (1980) investigated the accommodation and formation of  $\{11\bar{2}1\}$  twins in cobalt single crystals by transmission electron microscopy after ultrasonic cavitation shock. They revealed that both  $< \mathbf{c} + \mathbf{a} >$  and  $< \mathbf{a} >$  slips on the  $\{11\bar{2}1\}$  twinning plane precede the  $\{11\bar{2}1\}$  twinning in matrix, which governs the nucleation of  $\{11\bar{2}1\}$  twins. Amouzou et al. (2016) modelled the hardening mechanisms in  $\alpha$ -titanium and found that the relative activity of  $< \mathbf{c} + \mathbf{a} >$  slip increases with the deformation. Deformation behaviour of  $\alpha$ -titanium at extreme strain rates indicates that prismatic slip dominated the beginning of plastic deformation while the contribution of  $< \mathbf{c} + \mathbf{a} >$  slip increased at large strains (Gurao et al., 2011). Salem et al. (2003) studied the three stages of work hardening in polycrystalline  $\alpha$ -titanium, and found that the critical resolved shear stresses for high-purity titanium were 37, 49 and 197 MPa for prism  $< \mathbf{a} >$ , basal  $< \mathbf{a} >$ , and pyramidal  $< \mathbf{c} + \mathbf{a} >$  slip, respectively (Salem et al., 2005). Generally,  $< \mathbf{a} >$ -type dislocations on prismatic plane are predominant and  $< \mathbf{c} >$ -type dislocations on prismatic plane are occasionally observed in titanium deformed at a variety of strain rates and temperatures (Song and Gray, 1995). Both the  $< \mathbf{a} >$ - and  $< \mathbf{c} + \mathbf{a} >$ -type dislocations on pyramidal plane incline to activate in titanium when subjected to high strain rate deformation. Chichili et al. (1998) observed  $< \mathbf{a} >$ -type dislocations on  $(10\bar{1}2)$  pyramidal planes only in specimens deformed at high strain rates. Wang et al. (2015) reported  $< \mathbf{c} + \mathbf{a} >$ -type dislocations on  $\{11\bar{2}2\}$  and  $\{10\bar{1}1\}$  pyramidal planes as titanium is shocked by SHPB with strain rate  $10^3 \text{ s}^{-1}$ . In summary, the activity of  $< \mathbf{c} + \mathbf{a} >$  dislocations on  $\{10\bar{1}1\}$  pyramidal planes is highly improved at high strain rate deformation (Chichili et al., 1998; Wang et al., 2015), which can act as sources to produce the twinning dislocations associated with Group II and attribute to the increased proportion of Group II double twins. Besides, the interaction between the incoming  $< \mathbf{a} >$  dislocations and twin boundary may result in the formation of  $< \mathbf{c} + \mathbf{a} >$  dislocations via dislocation transmission, as revealed by TEM (Wang and Agnew, 2016) and simulation (Fan et al., 2015; Gong et al., 2018) in Mg.

For Group IV, the intersection between the primary and secondary twinning planes aligns along  $< 2\bar{3}13 >$  direction, which does not lie in usual slip planes. NDD mechanism fails for their nucleation.

### 5. Conclusion

We conducted high strain rate ( $\sim 2600 \text{ s}^{-1}$ ) compression of high purity titanium along the extrusion direction using a split Hopkinson pressure bar (SHPB) device. 453  $\{11\bar{2}1\} \rightarrow \{11\bar{2}2\}$  double twins are observed in six grains, while  $\{11\bar{2}1\} \rightarrow \{11\bar{2}4\}$  double twinning does not take place at all. Crystallographic analysis enables the classification of  $\{11\bar{2}1\} \rightarrow \{11\bar{2}2\}$  double twins into Group I ( $29.5^\circ < \bar{1}100 >$ ), Group II ( $55^\circ < 5 \ 5 \ \bar{1}0 \ 3 >$ ), Group III ( $80.6^\circ < \bar{1}100 >$ ) and Group IV ( $86.8^\circ < \bar{5} \ 15 \ \bar{1}0 \ 3 >$ ) according to the misorientation angle and axis pair. Groups I and II dominate in the proportion of experimentally detected double twins while Group III and Group IV account for a small proportion.

To explore the activity of these double twins and the mechanisms, we account for these phenomena according to apparent Schmid factor (a-SF), modified deformation gradient accommodation (m-DGA), and twin nucleation via dislocation dissociation (NDD). Combining with experimental observations, a-SF analysis is able to explain the high proportion of Group I and Group II  $\{11\bar{2}1\} \rightarrow \{11\bar{2}2\}$  double twins and the low frequency of Group III and Group IV  $\{11\bar{2}1\} \rightarrow \{11\bar{2}2\}$  double twins, but cannot predict the

poor activity of  $\{11\bar{2}1\} \rightarrow \{11\bar{2}4\}$  double twins. m-DGA analysis demonstrates that the preferred secondary twin mode and corresponding variant would, to the greatest extent, relax plastic deformation associated with the primary twinning. Thus it is capable of predicting the high activity of  $\{11\bar{2}1\} \rightarrow \{11\bar{2}2\}$  double twins than  $\{11\bar{2}1\} \rightarrow \{11\bar{2}4\}$  double twins, as well as the prevalence of Group I and Group II  $\{11\bar{2}1\} \rightarrow \{11\bar{2}2\}$  double twins over the other Groups. NDD analysis cannot rule out  $\{11\bar{2}1\} \rightarrow \{11\bar{2}4\}$  double twinning because  $\{11\bar{2}4\}$  double twins can also be nucleated through dissociation of basal  $\langle a \rangle$  dislocation at the boundary of primary  $\{11\bar{2}1\}$  twins as revealed in (Xu et al., 2018). Regarding  $\{11\bar{2}1\} \rightarrow \{11\bar{2}2\}$  double twinning, NDD analysis suggests that Group I  $\{11\bar{2}1\} \rightarrow \{11\bar{2}2\}$  double twinning is evoked by basal  $\langle a \rangle$  dislocations while Group II  $\{11\bar{2}1\} \rightarrow \{11\bar{2}2\}$  double twinning is facilitated by pyramidal  $\langle c+a \rangle$  dislocations which is highly active at high strain rate.

## Acknowledgments

PZ thanks the financial support by the subject development fund of Chinese Academy of Engineering Physics (CAEP) (Grant No. 2015B0301070). SX and JW acknowledge the support by the US National Science Foundation (NSF) (CMMI-1661686). Numerical analysis was completed utilizing the Holland Computing Center of the University of Nebraska, which receives support from the Nebraska Research Initiative.

## References

- Akhtar, A., 1975. Basal slip and twinning in  $\alpha$ -titanium single crystals. *Metall. Trans. A* 6, 1105.
- Amouzou, K., Richeton, T., Roth, A., Lebyodkin, M., Lebedkina, T., 2016. Micromechanical modeling of hardening mechanisms in commercially pure  $\alpha$ -titanium in tensile condition. *Int. J. Plast.* 80, 222–240.
- Ardeljan, M., Beyerlein, I.J., Knezevic, M., 2017. Effect of dislocation density-twin interactions on twin growth in AZ31 as revealed by explicit crystal plasticity finite element modeling. *Int. J. Plast.* 99, 81–101.
- Austin, R.A., McDowell, D.L., 2011. A dislocation-based constitutive model for viscoplastic deformation of fcc metals at very high strain rates. *Int. J. Plast.* 27, 1–24.
- Bao, L., Zhang, Y., Schuman, C., Lecomte, J.-S., Philippe, M.-J., Zhao, X., Esling, C., 2013. Multiple twinning in pure hexagonal close-packed titanium. *J. Appl. Crystallogr.* 46, 1397–1406.
- Barnett, M.R., Keshavarz, Z., Beer, A.G., Ma, X., 2008. Non-Schmid behaviour during secondary twinning in a polycrystalline magnesium alloy. *Acta Mater.* 56, 5–15.
- Berghezian, A., Fourdeux, A., Amelinckx, S., 1961. Transmission electron microscopy studies of dislocations and stacking faults in a hexagonal metal: Zinc. *Acta Metall.* 9, 464–490.
- Beyerlein, I.J., Wang, J., Barnett, M.R., Tome, C.N., 2012. Double twinning mechanisms in magnesium alloys via dissociation of lattice dislocations. *Proc. R. Soc. A Math.* 468, 1496–1520.
- Bozzolo, N., Chan, L., Rollett, A.D., 2010. Misorientations induced by deformation twinning in titanium. *J. Appl. Crystallogr.* 43, 596–602.
- Chichili, D., Ramesh, K., Hemker, K., 1998. The high-strain-rate response of alpha-titanium: experiments, deformation mechanisms and modeling. *Acta Mater.* 46, 1025–1043.
- Christian, J.W., Mahajan, S., 1995. Deformation twinning. *Prog. Mater. Sci.* 39, 1–157.
- Chun, Y.B., Yu, S.H., Semiatin, S.L., Hwang, S.K., 2005. Effect of deformation twinning on microstructure and texture evolution during cold rolling of CP-titanium. *Mater. Sci. Eng., A* 398, 209–219.
- El Kadiri, H., Kapil, J., Oppedal, A., Hector, L., Agnew, S.R., Cherkaoui, M., Vogel, S., 2013. The effect of twin–twin interactions on the nucleation and propagation of twinning in magnesium. *Acta Mater.* 61, 3549–3563.
- Fan, H., Aubry, S., Arsenlis, A., El-Awady, J.A., 2015. The role of twinning deformation on the hardening response of polycrystalline magnesium from discrete dislocation dynamics simulations. *Acta Mater.* 92, 126–139.
- Ghaderi, A., Barnett, M.R., 2011. Sensitivity of deformation twinning to grain size in titanium and magnesium. *Acta Mater.* 59, 7824–7839.
- Ghosh, S., Shahba, A., Tu, X., Huskins, E.L., Schuster, B.E., 2016. Crystal plasticity FE modeling of Ti alloys for a range of strain-rates. Part II: image-based model with experimental validation. *Int. J. Plast.* 87, 69–85.
- Gong, M., Liu, G., Wang, J., Capolungo, L., Tomé, C.N., 2018. Atomistic simulations of interaction between basal  $\langle a \rangle$  dislocations and three-dimensional twins in Magnesium. *Acta Mater.* 155, 187–198.
- Gurao, N., Kapoor, R., Suwas, S., 2011. Deformation behaviour of commercially pure titanium at extreme strain rates. *Acta Mater.* 59, 3431–3446.
- Hazeli, K., Kannan, V., Kingstedt, O., Ravichandran, G., Ramesh, K., 2018. Deformation Twin Nucleation and Twin Variant Selection in Single crystal Magnesium as a Function of Strain Rate. *arXiv preprint arXiv:1801.10252*.
- Hong, S.-G., Park, S.H., Lee, C.S., 2010. Role of  $\{10\text{-}12\}$  twinning characteristics in the deformation behavior of a polycrystalline magnesium alloy. *Acta Mater.* 58, 5873–5885.
- Hong, S.-G., Park, S.H., Lee, C.S., 2011. Strain path dependence of  $\{10\text{-}12\}$  twinning activity in a polycrystalline magnesium alloy. *Scripta Mater.* 64, 145–148.
- Jin, S., Marthinsen, K., Li, Y., 2016. Formation of  $\{11\text{-}21\}$  twin boundaries in titanium by kinking mechanism through accumulative dislocation slip. *Acta Mater.* 120, 403–414.
- Jonas, J.J., Mu, S., Al-Samman, T., Gottstein, G., Jiang, L., Martin, É., 2011. The role of strain accommodation during the variant selection of primary twins in magnesium. *Acta Mater.* 59, 2046–2056.
- Juan, P.-A., Berbenni, S., Capolungo, L., 2012. Prediction of internal stresses during growth of first-and second-generation twins in Mg and Mg alloys. *Acta Mater.* 60, 476–486.
- Juan, P.-A., Berbenni, S., Barnett, M., Tomé, C., Capolungo, L., 2014. A double inclusion homogenization scheme for polycrystals with hierarchical topologies: application to twinning in Mg alloys. *Int. J. Plast.* 60, 182–196.
- Khan, A.S., Yu, S., 2012. Deformation induced anisotropic responses of Ti-6Al-4V alloy. Part I: Experiments. *Int. J. Plast.* 38, 1–13.
- Khan, A.S., Suh, Y.S., Kazmi, R., 2004. Quasi-static and dynamic loading responses and constitutive modeling of titanium alloys. *Int. J. Plast.* 20, 2233–2248.
- Khan, A.S., Kazmi, R., Farrokh, B., 2007. Multiaxial and non-proportional loading responses, anisotropy and modeling of Ti-6Al-4V titanium alloy over wide ranges of strain rates and temperatures. *Int. J. Plast.* 23, 931–950.
- Khan, A.S., Yu, S., Liu, H., 2012. Deformation induced anisotropic responses of Ti-6Al-4V alloy Part II: a strain rate and temperature dependent anisotropic yield criterion. *Int. J. Plast.* 38, 14–26.
- Lainé, S.J., Knowles, K.M., 2015.  $\{11\text{-}24\}$  deformation twinning in commercial purity titanium at room temperature. *Philos. Mag.* A 95, 2153–2166.
- Mendelson, S., 1969. Zonal dislocations and twin lamellae in h.c.p. metals. *Mater. Sci. Eng.* 4, 231–242.
- Mendelson, S., 1970. Dislocation dissociations in hcp metals. *J. Appl. Phys.* 41, 1893.
- Morrow, B.M., Cerreta, E.K., McCabe, R.J., Tome, C.N., 2014a. Toward understanding twin–twin interactions in hcp metals: utilizing multiscale techniques to characterize deformation mechanisms in magnesium. *Mater. Sci. Eng., A* 613, 365–371.
- Morrow, B.M., McCabe, R.J., Cerreta, E.K., Tomé, C.N., 2014b. Observations of the atomic structure of tensile and compressive twin boundaries and twin–twin interactions in zirconium. *Metall. Mater. Trans.* 45, 5891–5897.
- Mu, S., Jonas, J.J., Gottstein, G., 2012. Variant selection of primary, secondary and tertiary twins in a deformed Mg alloy. *Acta Mater.* 60, 2043–2053.

- Mullins, S., Patchett, B., 1981. Deformation microstructures in titanium sheet metal. *Metall. Trans. A* 12, 853–863.
- Nemat-Nasser, S., Guo, W., Cheng, J., 1999. Mechanical properties and deformation mechanisms of a commercially pure titanium. *Acta Mater.* 47, 3705–3720.
- Obersson, P., Ankem, S., 2009. The effect of time-dependent twinning on low temperature ( $< 0.25 T_m$ ) creep of an alpha-titanium alloy. *Int. J. Plast.* 25, 881–900.
- Park, S.H., Hong, S.-G., Lee, J.H., Lee, C.S., 2012. Multiple twinning modes in rolled Mg–3Al–1Zn alloy and their selection mechanism. *Mater. Sci. Eng., A* 532, 401–406.
- Partridge, P.G., 1967. The crystallography and deformation modes of hexagonal close-packed metals. *Metall. Rev.* 12, 169–194.
- Proust, G., Tomé, C., Kaschner, G., 2007. Modeling texture, twinning and hardening evolution during deformation of hexagonal materials. *Acta Mater.* 55, 2137–2148.
- Qin, H., Jonas, J.J., 2014. Variant selection during secondary and tertiary twinning in pure titanium. *Acta Mater.* 75, 198–211.
- Qin, H., Jonas, J.J., Yu, H., Brodusich, N., Gauvin, R., Zhang, X., 2014. Initiation and accommodation of primary twins in high-purity titanium. *Acta Mater.* 71, 293–305.
- Roth, A., Lebyodkin, M.A., Lebedkina, T.A., Lecomte, J.S., Richeton, T., Amouzou, K.E.K., 2014. Mechanisms of anisotropy of mechanical properties of  $\alpha$ -titanium in tension conditions. *Mater. Sci. Eng., A* 596, 236–243.
- Salem, A.A., Kalidindi, S.R., Doherty, R.D., 2003. Strain hardening of titanium: role of deformation twinning. *Acta Mater.* 51, 4225–4237.
- Salem, A., Kalidindi, S., Semiatin, S., 2005. Strain hardening due to deformation twinning in  $\alpha$ -titanium: constitutive relations and crystal-plasticity modeling. *Acta Mater.* 53, 3495–3502.
- Sandlöbes, S., Friák, M., Neugebauer, J., Raabe, D., 2013. Basal and non-basal dislocation slip in Mg–Y. *Mater. Sci. Eng.* 576, 61–68.
- Shahba, A., Ghosh, S., 2016. Crystal plasticity FE modeling of Ti alloys for a range of strain-rates. Part I: a unified constitutive model and flow rule. *Int. J. Plast.* 87, 48–68.
- Shi, Z.-Z., Zhang, Y., Wagner, F., Richeton, T., Juan, P.-A., Lecomte, J.-S., Capolungo, L., Berbenni, S., 2015. Sequential double extension twinning in a magnesium alloy: combined statistical and micromechanical analyses. *Acta Mater.* 96, 333–343.
- Sim, G.-D., Kim, G., Lavenstein, S., Hamza, M.H., Fan, H., El-Awady, J.A., 2018. Anomalous hardening in magnesium driven by a size-dependent transition in deformation modes. *Acta Mater.* 144, 11–20.
- Song, S., Gray III, G., 1995. Structural interpretation of the nucleation and growth of deformation twins in Zr and Ti—II. Tem study of twin morphology and defect reactions during twinning. *Acta Metall.* 43, 2339–2350.
- Stanford, N., Carlson, U., Barnett, M., 2008. Deformation twinning and the Hall–Petch relation in commercial purity Ti. *Metall. Mater. Trans.* 39, 934–944.
- Thornburg, D., Piehler, H., 1975. An analysis of constrained deformation by slip and twinning in hexagonal close packed metals and alloys. *Metall. Trans. A* 6, 1511.
- Tirry, W., Nixon, M., Cazacu, O., Coghe, F., Rabet, L., 2011. The importance of secondary and ternary twinning in compressed Ti. *Scripta Mater.* 64, 840–843.
- Vaidya, S., Mahajan, S., 1980. Accommodation and formation of  $\{11\text{-}21\}$  twins in Co single crystals. *Acta Metall.* 28, 1123–1131.
- Wang, F., Agnew, S.R., 2016. Dislocation transmutation by tension twinning in magnesium alloy AZ31. *Int. J. Plast.* 81, 63–86.
- Wang, L., Barabash, R., Bieler, T., Liu, W., Eisenlohr, P., 2013. Study of  $\{11\text{-}21\}$  twinning in  $\alpha$ -Ti by EBSD and laue microdiffraction. *Metall. Mater. Trans.* 44, 3664–3674.
- Wang, J., Yu, Q., Jiang, Y., Beyerlein, I.J., 2013a. Twinning-associated boundaries in hexagonal close-packed metals. *JOM (J. Occup. Med.)* 66, 95–101.
- Wang, J., Beyerlein, I.J., Tomé, C.N., 2013b. Reactions of lattice dislocations with grain boundaries in Mg: implications on the micro scale from atomic-scale calculations. *Int. J. Plast.* 56, 156–172.
- Wang, T., Li, B., Li, M., Li, Y., Wang, Z., Nie, Z., 2015. Effects of strain rates on deformation twinning behavior in  $\alpha$ -titanium. *Mater. Char.* 106, 218–225.
- Won, J.W., Kim, D., Hong, S.-G., Lee, C.S., 2016. Anisotropy in twinning characteristics and texture evolution of rolling textured high purity alpha phase titanium. *J. Alloy. Comp.* 683, 92–99.
- Wyatt, Z., Joost, W., Zhu, D., Ankem, S., 2012. Deformation mechanisms and kinetics of time-dependent twinning in an  $\alpha$ -titanium alloy. *Int. J. Plast.* 39, 119–131.
- Xiang, M., Liao, Y., Wang, K., Lu, G., Chen, J., 2018. Shock-induced plasticity in semi-coherent  $\{111\}$  Cu–Ni multilayers. *Int. J. Plast.* 103, 23–38.
- Xie, K.Y., Alam, Z., Caffee, A., Hemker, K.J., 2016. Pyramidal I slip in c-axis compressed Mg single crystals. *Scripta Mater.* 112, 75–78.
- Xin, Y., Wang, M., Zeng, Z., Nie, M., Liu, Q., 2012. Strengthening and toughening of magnesium alloy by  $\{10\text{-}12\}$  extension twins. *Scripta Mater.* 66, 25–28.
- Xu, F., Zhang, X., Ni, H., Liu, Q., 2012.  $\{11\text{-}24\}$  deformation twinning in pure Ti during dynamic plastic deformation. *Mater. Sci. Eng., A* 541, 190–195.
- Xu, S., Liu, T., Chen, H., Miao, Z., Zhang, Z., Zeng, W., 2013. Reducing the tension–compression yield asymmetry in a hot-rolled Mg–3Al–1Zn alloy via multidirectional pre-compression. *Mater. Sci. Eng., A* 565, 96–101.
- Xu, S., Schuman, C., Lecomte, J.-S., 2016. Accommodative  $\{10\text{-}12\}$  twins at high angle grain boundaries in rolled pure titanium. *Scripta Mater.* 116, 152–156.
- Xu, S., Gong, M., Schuman, C., Lecomte, J.-S., Xie, X., Wang, J., 2017a. Sequential  $\{10\text{-}12\}$  twinning stimulated by other twins in titanium. *Acta Mater.* 132, 57–68.
- Xu, S., Gong, M., Xie, X., Liu, Y., Schuman, C., Lecomte, J.-S., Wang, J., 2017b. Crystallographic characters of  $\{11\text{-}22\}$  twin-twin junctions in titanium. *Phil. Mag. Lett.* 1–13.
- Xu, S., Toth, L.S., Schuman, C., Lecomte, J.-S., Barnett, M.R., 2017c. Dislocation mediated variant selection for secondary twinning in compression of pure titanium. *Acta Mater.* 124, 59–70.
- Xu, S., Gong, M., Jiang, Y., Schuman, C., Lecomte, J.-S., Wang, J., 2018. Secondary twin variant selection in four types of double twins in titanium. *Acta Mater.* 152, 58–76.
- Yang, Y., Wang, L., Zambaldi, C., Eisenlohr, P., Barabash, R., Liu, W., Stoudt, M., Crimp, M., Bieler, T., 2011. Characterization and modeling of heterogeneous deformation in commercial purity titanium. *JOM (J. Occup. Med.)* 63, 66.
- Yoo, M.H., 1981. Slip, twinning, and fracture in hexagonal close-packed metals. *Metall. Trans. A* 12, 409–418.
- Yoo, M.H., Morris, J.R., Ho, K.M., Agnew, S.R., 2002. Nonbasal deformation modes of HCP metals and alloys Role of dislocation source and mobility. *Metall. Mater. Trans.* 33A, 813–822.
- Yu, Q., Zhang, J., Jiang, Y., 2011. Direct observation of twinning–detwinning–retwinning on magnesium single crystal subjected to strain-controlled cyclic tension–compression in  $[0001]$  direction. *Phil. Mag. Lett.* 91, 757–765.
- Yu, Q., Wang, J., Jiang, Y., McCabe, R.J., Li, N., Tomé, C.N., 2014a. Twin–twin interactions in magnesium. *Acta Mater.* 77, 28–42.
- Yu, Q., Wang, J., Jiang, Y., McCabe, R.J., Tomé, C.N., 2014b. Co-zone  $\{10\text{-}12\}$  twin interaction in magnesium single crystal. *Mater. Res. Lett.* 2, 82–88.
- Yu, Q., Jiang, Y., Wang, J., 2015. Cyclic deformation and fatigue damage in single-crystal magnesium under fully reversed strain-controlled tension–compression in the  $[10\text{-}10]$  direction. *Scripta Mater.* 96, 41–44.
- Zambaldi, C., Zehnder, C., Raabe, D., 2015. Orientation dependent deformation by slip and twinning in magnesium during single crystal indentation. *Acta Mater.* 91, 267–288.
- Zecevic, M., Beyerlein, I.J., Knezevic, M., 2018. Activity of pyramidal I and II  $< c + a >$  slip in Mg alloys as revealed by texture development. *J. Mech. Phys. Solid.* 111, 290–307.
- Zhou, P., Xiao, D., Jiang, C., Sang, G., Zou, D., 2017. Twin interactions in pure Ti under high strain rate compression. *Metall. Mater. Trans.* 48, 126–138.